ADVANCED FUNCTIONAL MATERIALS
www.afm-journal.de

Heterogeneous Integration of Graphene and HfO_2 Memristors

Urška Trstenjak, Kalle Goß, Alexander Gutsche, Janghyun Jo, Marcus Wohlgemuth, Rafal E. Dunin-Borkowski, Felix Gunkel, and Regina Dittmann**

The past decade has seen a growing trend toward utilizing (quasi) van der Waals growth for the heterogeneous integration of various materials for advanced electronics. In this work, pulsed-laser deposition is used to grow HfO_2 thin films on graphene/SiO_2/Si. As graphene is easily damaged under standard oxide-film deposition conditions, the process needs to be adjusted to minimize the oxidation and the collision-induced damage. A systematic study is conducted in order to identify the crucial deposition parameters for diminishing the defect concentration in the graphene interlayer. For evaluating the quality of graphene, it is mainly relied on data obtained from Raman spectroscopy, using approaches beyond the Tuinstra-Koenig relation. The results show that the defects are mainly a consequence of the high kinetic energy of the plasma-plume particles. Using a relatively high Ar process pressure, a sufficiently low defect concentration is ensured, without compromising the quality of the HfO_2 thin film. This enabled us to successfully prepare memristive devices with a filamentary type of switching, utilizing the graphene layer as a bottom electrode. The findings of this study can be easily transferred to other systems for the development of oxide electronic devices.

1. Introduction

Memristive devices or resistive random-access memories represent non-volatile, fast, low-power and cost-effective technology, emerging as a leading candidate to replace flash memory for a broad range of applications, such as in high-density memory, low-power Internet-of-Things devices, neuromorphic computing, sensory and security applications, etc.[1–5] Cointegration of oxides with 2D materials,[5,6] such as graphene, opens up the possibility to access an even wider variety of functional properties, ranging from sensory applications to electronics and optoelectronics. To this end, besides the compatibility of processing pressure and temperature, also interdiffusion and possible damage caused by high energetic particles have to be circumvented.

Thin-film hafnium oxide (HfO_2) is receiving a lot of research attention owing to its memristive as well as its ferroelectric properties.[7,8] In fact, HfO_2 is one of the most researched switching oxide materials owing to its scalability and compatibility with complementary metal-oxide-semiconductor technology.[9] It has been shown that amorphous HfO_2,[10] as well as other amorphous oxides such as Al_2O_3[11–13] have been successfully grown on graphene by means of atomic layer deposition, without significantly damaging the graphene. Crystalline thin films offer additional degrees of freedom for tailoring their properties, as compared to their amorphous counterparts, thereby expanding the window for potential applications. However, the synthesis of crystalline (and especially epitaxial) thin films directly on Si substrates usually entails intricate interface engineering and rigorous optimization of the deposition conditions.[14,15]

Crystalline thin films have also been successfully integrated with Si via the use of a 2D material, such as graphene as a buffer layer.[15–18] Graphene serves as a diffusion barrier, preventing the interfacial reactions at the high temperatures required for crystallization.[18] Owing to the 2D character of the template and the 3D character of the thin film material, quasi van der Waals (vdW) type of growth is realized.[17,19] This type of bonding offers several important advantages compared to conventional (oxide) epitaxy, including: i) dislocation-free strain relaxation mechanism,[20] and ii) possibility to delaminate the film

U. Trstenjak, K. Goß, A. Gutsche, M. Wohlgemuth, F. Gunkel, R. Dittmann
Peter Grünberg Institute 7
Forschungszentrum Jülich GmbH
52428 Jülich, Germany
E-mail: urska.trstenjak@ijs.si; r.dittmann@fz-juelich.de
U. Trstenjak
Advanced Materials Department
Jožef Stefan Institute
Ljubljana 1000, Slovenia
K. Goß, A. Gutsche, M. Wohlgemuth, F. Gunkel, R. Dittmann
Jülich-Aachen Research
Alliance (JARA-FIT)
52428 Jülich, Germany
J. Jo, R. E. Dunin-Borkowski
Ernst Ruska-Centre for Microscopy and Spectroscopy with Electrons
Forschungszentrum Jülich GmbH
52428 Jülich, Germany

The ORCID identification number(s) for the author(s) of this article can be found under https://doi.org/10.1002/adfm.202309558

DOI: 10.1002/adfm.202309558

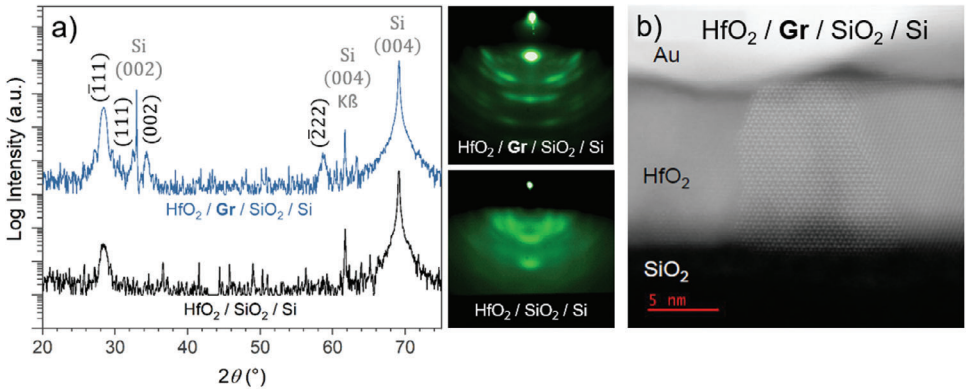

Figure 1. a) X-ray diffractograms (left) and RHEED patterns (right) of the HfO_2 thin films deposited on substrates with (top) and without (bottom) the graphene buffer layer at (p(Ar) = 0.1 mbar, fluence = 2 J cm^{-2}, target-to-substrate distance (TSD) = 51 mm and T = 830 °C. RHEED patterns were taken along Si[100]. b) HAADF-STEM micrograph of the HfO_2/Gr/SiO_2/Si heterostructure. Here, the HfO_2 was grown at slightly varied growth parameters (p(Ar) = 0.2 mbar, fluence = 2 J cm^{-2}, TSD = 51 mm and T = 750 °C), which, based on the comparable XRD data (not shown here) and the 3D growth mechanism, are not expected to significantly affect the crystallization behavior. The Gr layer could not be identified in this micrograph, either due to (i) damage induced by the focused-ion-beam (FIB) used to prepare the cross-section lamella, or (ii) due to damage induced by the PLD process itself, the latter being the more likely cause.

to create a free-standing membrane or to transfer it to a support of choice.[21–25] Nevertheless, the path to achieve such heterostructures is complex. The key challenge to overcome is the inherent incompatibility between the stability window of the graphene and the synthesis window for oxide thin films. In other words, the oxidizing conditions at high temperatures usually required to produce stoichiometric thin films of high crystalline quality, can lead to the decomposition of the graphene.[17,18,26] Furthermore, the highly energetic particles in deposition techniques such as sputtering and pulsed-laser deposition (PLD) are also likely to damage the graphene-based template.[21] Both of these effects can be mitigated by the use of an inert gas, such as Ar, as process gas. The influence of different *p*(Ar) on the defect concentration has not been studied yet. Additionally, the role of the oxygen-containing species from the target material in the potential oxidation of the graphene-based template has not been elucidated yet. These insights are required to enable the selection of the appropriate processing conditions.

For this purpose, we have conducted a systematic study of the influence of different PLD parameters, including *p*(Ar), on the quality of graphene-based templates. We used Raman spectroscopy to evaluate the constitution of graphene and the defect concentration, using approaches beyond the widely used Tuinstra-Koenig relation, by exploiting accurate modelling of the Raman peak shapes. We used SiO_2/Si substrates to avoid overlap of substrate and film signal in the Raman spectra, and in order to unambiguously determine the influence of graphene on the HfO_2 film crystallization. The properties of the HfO_2 thin films grown at these conditions were analyzed in parallel to ensure a balance between the graphene and HfO_2 film quality. The defined set of parameters that is presented, enabled us to prepare memristive devices using the graphene as bottom electrode. The presented approach builds the foundation for the growth of various complex oxides and heterostructures on graphene using advantages offered by PLD.

2. Results and Discussion

2.1. Influence of Graphene on HfO_2 Growth

First, in order to determine the influence of graphene on the growth of the oxide thin film, HfO_2 was deposited onto SiO_2/Si substrates with and without the graphene interlayer, using the same exemplary PLD parameters with relatively high partial *p*(Ar). X-ray diffraction (XRD) and reflection high-energy electron diffraction (RHEED) results shown in panel a) of **Figure 1**, clearly demonstrate the important role of graphene in establishing highly crystalline growth. While the sample without graphene exhibits a single orientation in the X-ray diffractogram, the peak shape and intensity point to poor crystallization of the film. This is corroborated by the RHEED, where a blurry pattern is observed for this sample. On the other hand, the RHEED pattern of the sample grown with graphene, exhibits clear dashed rings, indicative of a crystalline textured film. Despite the improved crystalline quality of the HfO_2 film, brought about by the graphene interlayer, which acts as a diffusion barrier for Si,[27] no intensity oscillations were observed with RHEED during the growth, indicating the growth mode was 3D, as expected for textured films. The XRD results reveal that both films crystallized in the thermodynamically stable monoclinic phase, with the preferential ($\bar{1}11$) orientation. Using scanning transmission electron microscopy (STEM), nanosized (5 – 10 nm) grains were observed throughout the HfO_2/graphene (Gr)/SiO_2 /Si sample. A high-angle annular dark field (HAADF) STEM image of the sample is shown in panel b) of Figure 1.

2.2. Optimization of the Growth Parameters to Minimize the Defect Concentration in the Graphene

As explained in the introduction, the growth of thin films on graphene has been shown to induce damage in the graphene layer. Defects could be formed owing to the high kinetic energy of the arriving particles. Moreover, at high temperatures,

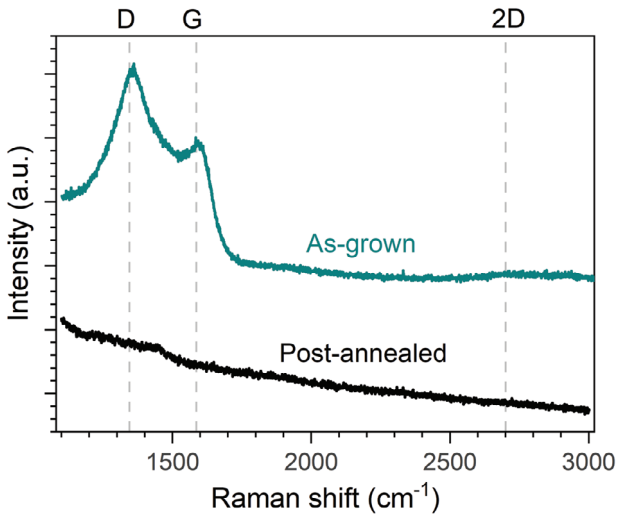

Figure 2. Raman spectra of a HfO_2/Gr/SiO_2/Si sample grown in Ar atmosphere, before (top) and after (bottom) post-annealing at T = 750 °C in p(O_2) = 0.2 mbar.

required for the growth of crystalline hafnia, in the presence of oxygen–either originating from the background gas during the growth or from the ceramic target–the graphene will oxidize. In order to minimize the defect concentration, we have adjusted several deposition parameters. Based on the knowledge obtained from literature reports[17,18] and our preliminary studies, all films were grown without the presence of oxygen gas to avoid the oxidation of the graphene. Furthermore, our results show that even post-annealing a sample grown in Ar atmosphere leads to a complete loss of Raman signature (*D*, *G*, and *2D* bands) for graphene, as shown in **Figure 2**. Therefore, the main efforts in the parametric studies were directed at reducing the kinetic energy of the impinging particles and at minimizing the chemical reactions between the materials at the interface.

The signature features in the Raman spectra of pristine graphene are the *G* band and the *2D* band. In the presence of defects, the D band is activated as well. The calculation of the intensity ratio of the *D* and *G* bands (I_D/I_G) is the most commonly used approach for evaluating the quality of graphene (after thin-film deposition).[17,19,26] It is based on the Tuinstra-Koenig relation ($I_D/I_G = C(\lambda)/L_a$, where $C(\lambda)$ is a proportionality constant that depends on the excitation laser wavelength, and L_a is the size of crystalline sp^2 clusters or the in-plane correlation length).[28] This approach has some limitations, which will be discussed in Subsection 2.3, where in-depth analysis will be presented. Nevertheless, for the initial growth-parameter studies, we also used the I_D/I_G ratio along with the full-widths-at-half-maxima (FWHM) of the two peaks, and I_{2D} to estimate the defect concentration in the samples after the PLD growth of the HfO_2 films. It is of paramount importance to also take into consideration the latter two parameters. 1) The FWHM increases with increasing defect concentration. 2) The *2D* band (together with the *G* band) is a signature of graphitic sp^2 materials.[29] Therefore, its absence points to a lack of sp^2 bonds in the sample and thereby to a high defect concentration, regardless of the I_D/I_G ratio for a given sample.

First, we measured as-transferred monolayer graphene on Si/SiO_2. As shown in Figure S1 (Supporting Information), the *D* band is absent, attesting to the high quality of the as-transferred layer. The $I_{2D}/I_G \approx 2$ confirms that the graphene consists of a single layer. The Raman spectrum changes drastically after deposition of HfO_2, as shown in Figure 2, where the "As-grown" sample was deposited in Ar atmosphere. The *2D* band is no longer visible, while a very strong *D* band appears. The *D* and *G* bands have high FWHMs. This is indicative of graphene with a very high defect concentration.

The first set of results of the PLD parametric studies are shown in **Figure 3**. In order to reduce the flux of the particles in the plasma plume, we varied the laser fluence values from 1.2 J cm^{-2}–3 J cm^{-2}. All three films were deposited in *p*(Ar) = 0.1 mbar. Representative Raman spectra are shown in panel a). The defect density was relatively high for all three fluence values. While I_D/I_G was the highest in the sample grown using the lowest fluence, namely 1.2 J cm^{-2}, the FWHM were the lowest and the I_{2D} was the highest in this sample. This indicates that at 1.2 J cm^{-2}, the defect density is the lowest. Nevertheless, a fluence of 2.0 J cm^{-2} was selected for further experiments, owing to the results of the RHEED and AFM analysis (Figure 3b), which showed that the crystallinity and texturing was the highest for the sample prepared using a fluence value of 2.0 J cm^{-2}, which also exhibited a moderate root-mean-square (RMS) roughness. The RMS values are inversely proportional to the thickness, indicating that the roughness is directly related to the growth parameters (fluence).

Next, we varied the target-to-substrate distance (Figure S2, Supporting Information, panel a)) in order to decrease the kinetic energy of the particles arriving to the substrate surface. We did not find significant improvement by increasing the distance. In order to suppress the chemical reaction at the interface, we also tried decreasing the deposition temperature (Figure S2, panel b)). The I_D/I_G was again similar for both samples. Therefore, these parameters are not crucial in view of the conservation of graphene quality.

We hypothesized that the high defect density was a consequence of the high kinetic energy of the plasma-plume particles. As the most efficient way to reduce the kinetic energy of the impinging particles is to increase the process pressure, we conducted a pressure series, where we varied the Ar partial pressure in the chamber (**Figure 4**). With increasing pressure, the following trends are observed in Raman spectroscopy (panel a)): the *2D* band intensifies, indicating a larger quantity of sp^2-hybridized bonds; the *D* and *G* bands intensify, their FWHM decrease, indicating higher-quality graphene layers; the I_D/I_G ratio does not change significantly up to *p*(Ar) = 0.1 mbar. For *p*(Ar) = 0.2 mbar, the ratio is the highest. However, as the FWHM are the lowest, and there is a pronounced *2D* peak – this indicates the defect density is the lowest in this sample (see Section 2.3 for detailed explanation). Process pressures higher than 0.2 mbar were not used, due to low deposition rate. AFM micrographs of the samples are shown in the Supporting Information (Figure S3, Supporting Information). Their surface quality is comparable. The RMS roughness is the lowest in samples grown at intermediate pressures, as shown in Figure 4b). The X-ray diffractograms of the samples are shown in panels c) and d) of Figure 4. All peaks can be assigned to the thermodynamically stable monoclinic phase. The films

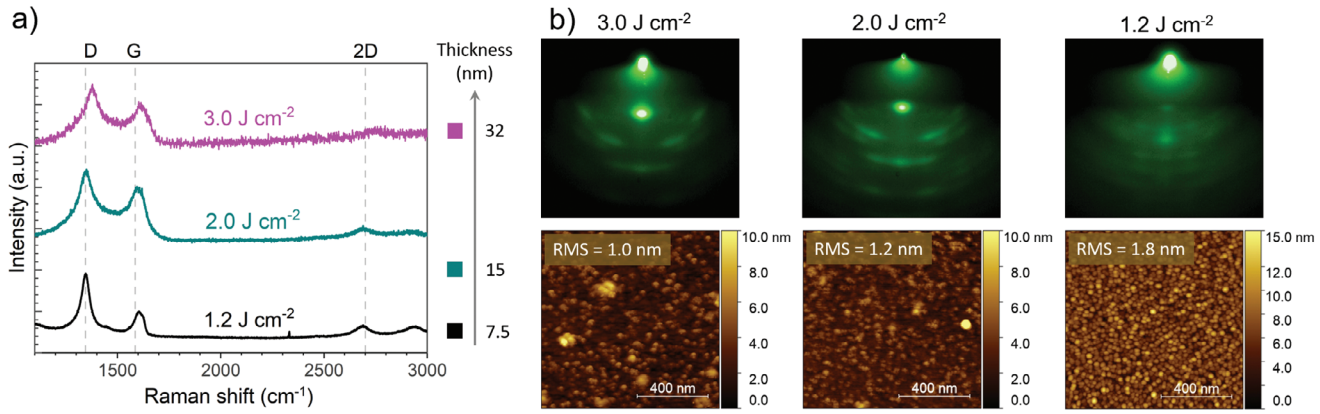

Figure 3. a) Raman spectra and b) RHEED and AFM images of samples synthesized using different fluence values.

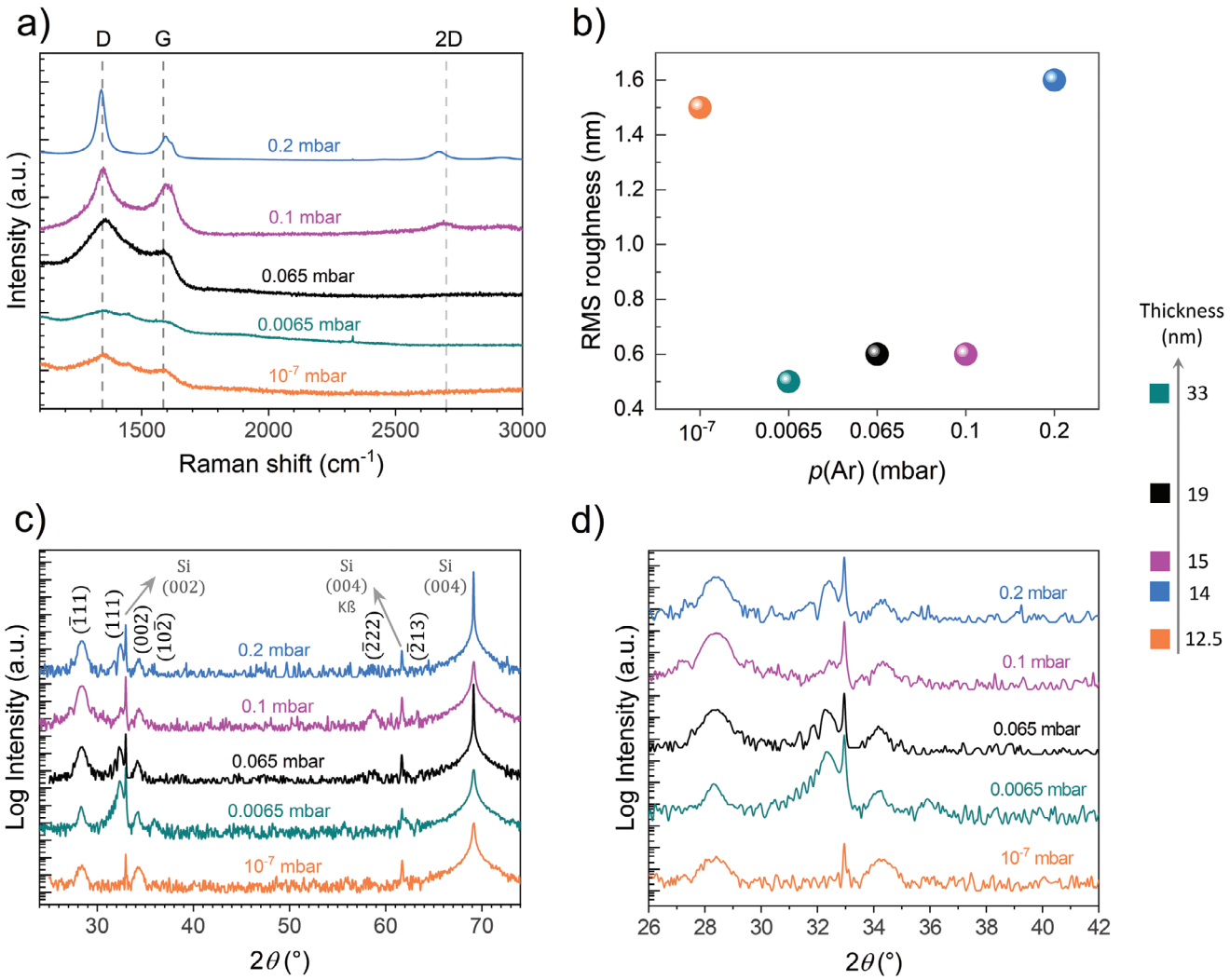

Figure 4. a) Raman spectra, b) RMS roughness calculated from AFM images and c) X-ray diffractograms for samples synthesized at different p(Ar). In panel d) the 2θ region around the first-order reflections is enlarged for better visibility of the thickness oscillations.

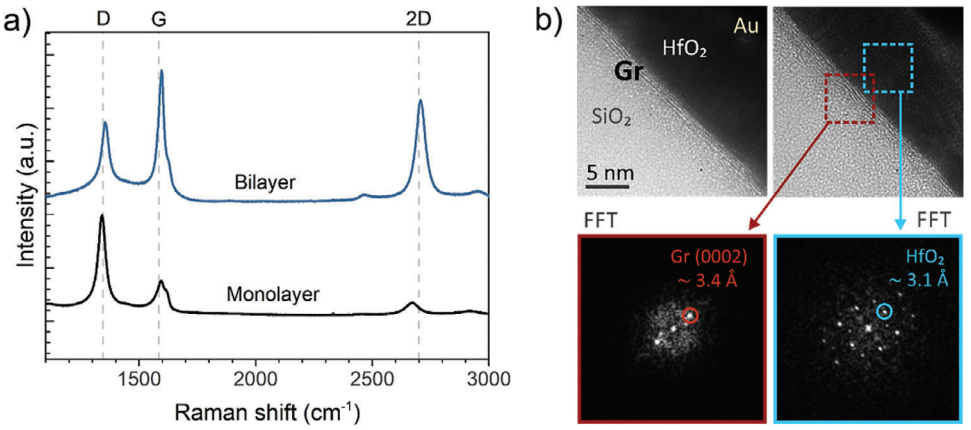

Figure 5. a) Raman spectra for samples synthesized on ML and BL graphene interlayers. b) HR-TEM micrographs of HfO_2 thin films grown on BL Gr/SiO_2/Si and the FFTs of the regions where Gr and HfO_2 are expected.

exhibit some variation in crystallographic out-of-plane texture. The crystalline quality and texturing do not seem to be related to the film thickness (scale shown on the right). The differences in the thickness were due to the different scattering rates at different pressures and the inability to monitor the film thickness in situ, owing to the absence of intensity oscillations in RHEED. On the other hand, thickness oscillations are present in the X-ray diffractograms (see panel d)), attesting to the high quality of the films.

In order to try and further reduce the defect concentration, we also focused on suppressing the oxidation process by growing the film in reducing atmosphere (Ar with 4% H_2) and using a faster cooling rate. Based on the Raman data (Figure S4, Supporting Information), these parameters do not have a significant influence on the graphene quality.

According to literature reports[21,30] bilayer (BL) graphene is significantly more resilient than monolayer (ML) graphene. Therefore, we used the optimized deposition parameters (p(Ar) = 0.2 mbar, fluence = 2 J cm^{-2}, TSD = 51 mm and T = 750 °C) to grow a HfO_2 thin film on BL graphene (Gr)/SiO_2/Si. A comparison of Raman spectroscopy measurements on HfO_2 films grown on ML and BL Gr is shown **Figure** 5a). The I_D/I_G ratio is significantly lower in the BL sample. Importantly, the intensity of the 2D band is also highly increased. Nevertheless, the sample with BL Gr is also highly sensitive to oxidation. As shown in Figure S5 (Supporting Information), after post-annealing, all Raman bands characteristic for graphene are absent, indicating the BL Gr fully decomposed during the post-processing step.

We have summarized the impact of all varied synthesis parameters on the quality of the graphene and HfO_2 films in Table S1 (Supporting Information).

We analyzed the heterostructures using TEM. In the BL sample, graphene layers were observed between SiO_2 and the HfO_2 thin film (Figure 5b). The identification of graphene was confirmed by fast fourier transform (FFT) patterns of the HR-TEM images. Diffraction peaks corresponding to the (0002) planes of graphene were observed. We have also found several regions, where graphene was absent. These could be the regions where the graphene got damaged during PLD growth, or it could occur during the FIB lamella preparation.

2.3. Detailed Analysis of the Raman Spectroscopy Data

While the Tuinstra-Koenig relation can be used to reliably determine the defect concentration in samples with relatively small degree of disorder, for large disorders the relation fails and I_D/I_G actually starts to monotonically decrease.[31] Therefore, a more holistic approach is called for when interpreting Raman data of graphene-based samples with (expected) high defect concentrations.[31,32] The *G* and *2D* peaks in the Raman spectrum satisfy the Raman selection rule, but the Raman-forbidden defect-activated bands can also appear in the spectrum. Here, the defect provides the missing momentum to satisfy the momentum conservation in the Raman scattering process.[28] These bands are activated by grain boundaries, in-plane substitutional heteroatoms or vacancies, amorphization, hydrogenation or other types of Raman-active defects. In addition to the widely known *D* band, other defect-activated bands such as: *D′*, *D″*, *D**, and *D*** can also appear in close spectral vicinity of the intrinsic *G* band (cf. **Table** 1). Charged impurities, intercalants, strain and perfect zig-zag edges do not generate a *D* peak. For analyzing such "silent" defects, other Raman signatures should be used. Zig-zag edges affect the *G* peak shape, while the rest influence both the *G* and *2D* peaks. Some defects are altogether Raman silent. Adsorbed charged impurities are not expected to give detectable *D* and *D′* peaks.

The positions and descriptions of the different Raman bands for graphene that appear in the region of interest (first order peaks; between 1100 cm^{-1} and 1800 cm^{-1}) are listed in Table 1. From the positions it is clear that the regions of the *D* and especially *G* band can actually be composed of several peaks. For better understanding of the defect types, a deconvolution of the contributions is necessary. It is also important to consider any potential contributions from the substrate and any impurities. Therefore, for our samples, we have also considered peaks that belong to the Si substrate and small poly-methyl-metacrylate (PMMA) particulates that might remain on the Gr surface due to

Table 1. Description of Raman active bands in the region of interest.

Band abbreviation	Raman shift (cm^{-1})	Description
D	1345	Disorder band or the defect band, related to the ring breathing mode from sp^2 carbon rings – active if adjacent to a graphene edge or a defect
G	1585	Primary mode in graphene and graphite; planar configuration sp^2- bonded carbon; Position sensitive to doping and strain
*D**	1150-1200	sp^3-rich phase of disordered amorphous carbons
D″	1500-1550	Broad peak; related to the amorphous phase, intensity is inversely related to the crystallinity
*D***	1500	Contributions from the phonon density of states in finite size graphitic crystals or due to C-H vibrations in hydrogenated carbons
D′	≈1610	Disorder induced feature due to crystal defects or double vacancy corresponding to pentagonal and octagonal rings
Si	≈1450	Third and fourth order scattering, respectively
PMMA	1450	Strongest bands; Residues on the samples′ surface

incomplete removal during the transfer process. We have added the peak positions for these two materials to Table 1. The curve fit for our sample prepared on ML Gr at $p(Ar) = 0.2$ mbar is shown in **Figure 6**. Looking at the spectrum as a whole, there was actually no detectable contribution from the Si substrate, while the PMMA did have a slight contribution to the background. A low-amplitude peak can be recognized at ≈1450 cm^{-1}. There were no detectable contributions from the *D** and *D*** bands, whereas the *D″* and *D′* bands could be fitted well into the G-band region. The appearance of the *D″* band indicates a certain degree of amorphization, and the *D′* band is a disorder-induced feature due to lattice defects,[33] arguably double vacancies, so-called 5-8-5 defects.[34] It has been shown[35] that the $I_D/I_{D'}$ ratio can be used to determine the type of defects in the graphene. For sp^3-type of defects, the ratio is ≈13, whereas for vacancy-type of defects, the ratio equals ≈7. Based on our fit shown in Figure 6, the ratio for this sample is ≈5, implying the defects are predominantly vacancy-type. The vacancies are likely a consequence of the impinging plasma-plume particles. On the other hand, the vacancies could result from the incorporation of C into the HfO_2 lattice, which stabilizes the nucleation of the thin film, as shown recently for the growth of HfO_2 nanoislands on highly ordered pyrolitic graphite (HOPG).[36]

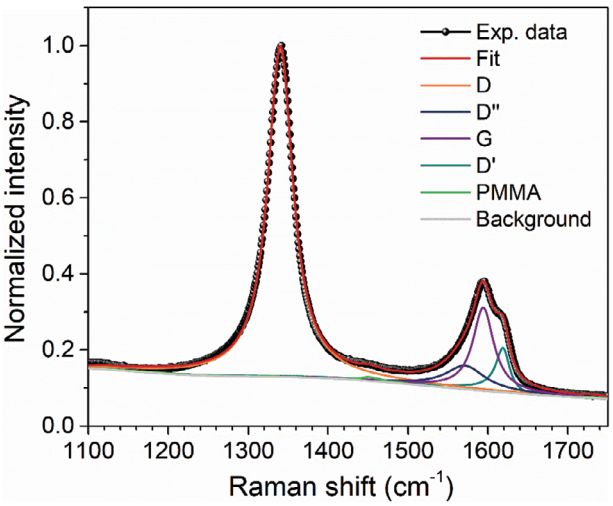

Figure 6. Raman spectrum fit for the sample prepared on ML Gr at p(Ar) = 0.2 mbar.

Our results indicate that using the selected growth conditions, the defect concentration in graphene can be limited. This enabled us to use these graphene layers as bottom electrode in metal-insulator-metal (MIM) device structures.

2.4. Device Configuration and *I–V* Measurements

In order to test the memristive behavior, we rely on an well-preserved graphene layer serving as bottom electrode of the device. The graphene layers with the higher defect concentration yielded insufficient in-plane conduction to serve as a bottom electrode, while the sample with the best graphene crystallinity also yielded a clear and accessible bottom electrode. The device configuration with ML graphene is shown in **Figure 7a**). In order to obtain a low-resistance metal-graphene contact,[37–39] we used a 1D/side contact to the graphene via Pt/Ti. Pt/Ti metal contact were used, as Ti-graphene contacts have been reported to exhibit relatively low contact resistivity.[39–41] Furthermore, Ti acts a oxygen getter, which scavanges oxygen from the HfO_2 and thereby reduces the forming voltage.[42,43] We first tested the resistance of the graphene layer (bottom-to-bottom contact) across the 10 mm × 10 mm sample. The obtained resistance values were ≈2 kΩ, which is comparable to the values we obtained for the as-transferred graphene (≈1–2 kΩ), indicating that the graphene was conserved sufficiently during the growth process to provide a well-defined bottom electrode for the devices. A representative current-votage (*I–V*) measurement of the MIM device is shown in Figure 7b).

Owing to the use of Ti as a top contact, which scavenged the oxygen, the HfO_2 thin film was highly depleted of oxygen, leading to a highly conductive layer, which did not exhibit any hysteresis (Figure 7b). This hypothesis was confirmed with TEM analysis, where the elemental maps and line profiles by energy-dispersive X-ray spectroscopy (EDX) showed significant overlap

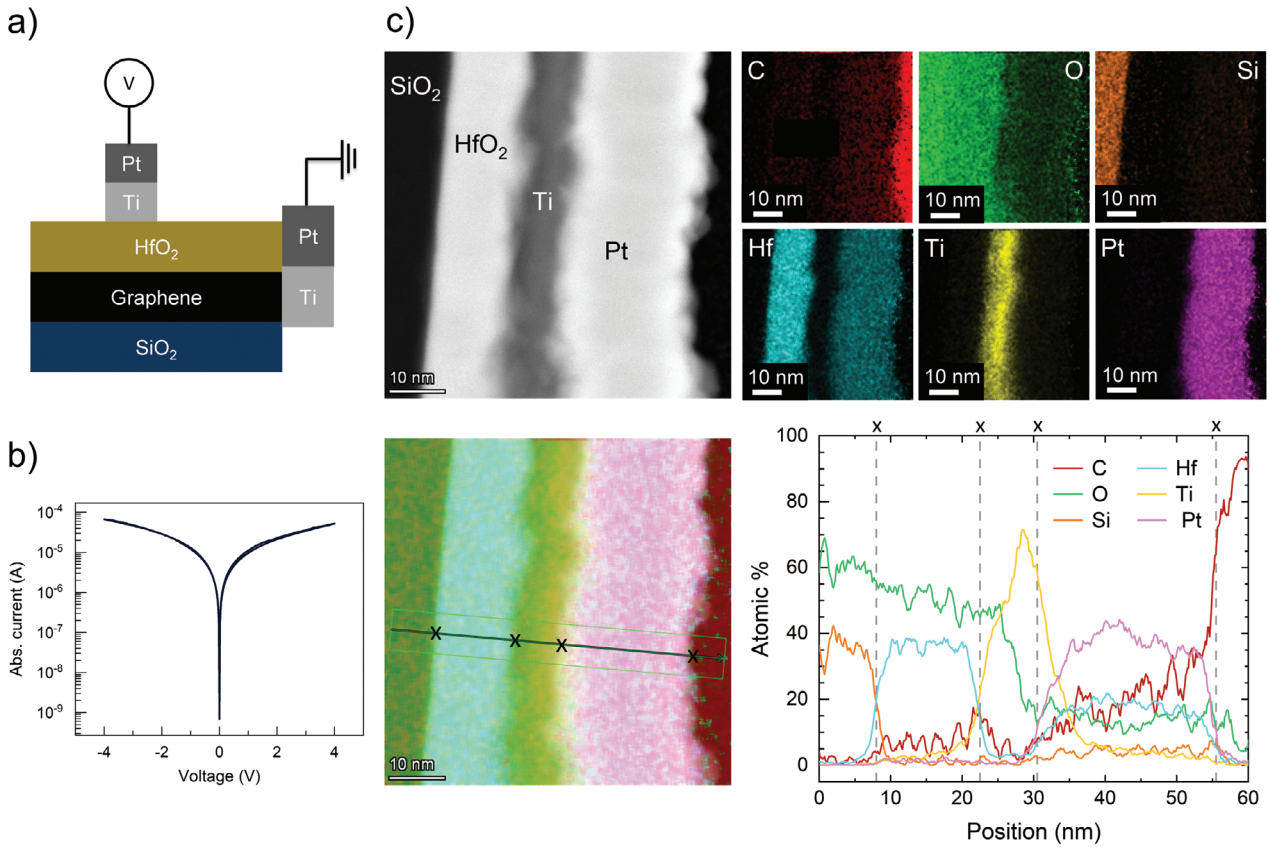

Figure 7. a) Schematic representation of the device configuration in side-view. b) *I–V* curve of the sample shown in panel a). c) TEM image and individual EDX elemental maps (top), and elemental map convolution with line profile of the device in cross-section (bottom). Interfaces, as identified on the map, are marked with "x". No interdiffusion was detected at the SiO_2/HfO_2 interface. The apparent high concentration of Hf in the Pt layer is an artefact, originating from Hf and Pt peaks overlap.

of O and Ti line profiles, indicating a part of the Ti layer is oxidized (Figure 7c).

Therefore, in the second configuration (**Figure** 8a), we used Pt as the top contact, instead of Ti. The graphene bottom electrode was contacted in a side-contact geometry. The electroforming step and the first cycle on a device with an area of 100 μm^2 are shown in panels b) and c), respectively. The cycling behavior (first 10 cycles is shown in Figure S6, Supporting Information. The *I–V* curves look very similar to typical filamentary switching in HfO_2 with a steep SET process and a gradual RESET process.[44,45] Due to the forming process performed at positive voltages, oxygen is released at the top Pt electrode, causing a reduction of HfO_2 at the top electrode. As a result, the Schottky barrier at the top electrode is reduced compared to the bottom causing the asymmetry required for bipolar switching.[46] The observed relatively high forming and switching voltages, have also been reported for memristive devices with pristine graphene (top) electrodes,[47,48] presumably owing to the relatively high series resistance (≈2 kΩ) of the graphene.

3. Conclusion

We have successfully synthesized crystalline HfO_2 thin films on graphene/SiO_2/Si templates via quasi van der Waals growth using PLD in Ar gas. Owing to the absence of substrate-induced strain in the quasi van der Waals type of growth, the films crystallized in the thermodynamically stable monoclinic phase, with the preferential ($\bar{1}11$) orientation. By analyzing the data obtained from Raman spectroscopy in detail, we found that the defects induced in the graphene by the HfO_2 deposition are predominantly sp^2-type, and are formed due to the high kinetic energy of the plasma-plume particles. Therefore, increasing the Ar process pressure is a good strategy for diminishing the defect concentration. The second approach is to use bilayer instead of monolayer graphene, as we have shown it is much less prone to damage. We confirmed the existence of BL Gr in the heterostructure using HR-TEM imaging.

In view of the three-stage classification of disorder proposed by Ferrari[49] for assessing the Raman spectra of carbons, most of the samples from our study exhibit Stage 2 type of disorder, where the I_D/I_G is decreased and the second-order peaks are not well defined or are completely absent. Therefore, the appearance of well-defined second-order peaks can be used as a solid and clear indicator of a diminished degree of disorder in such samples prepared by PLD.

To summarize, the results obtained in our study show that graphene can be used for the heterogeneous integration of crystalline HfO_2 thin films. Using Ar as process gas, the oxidation of

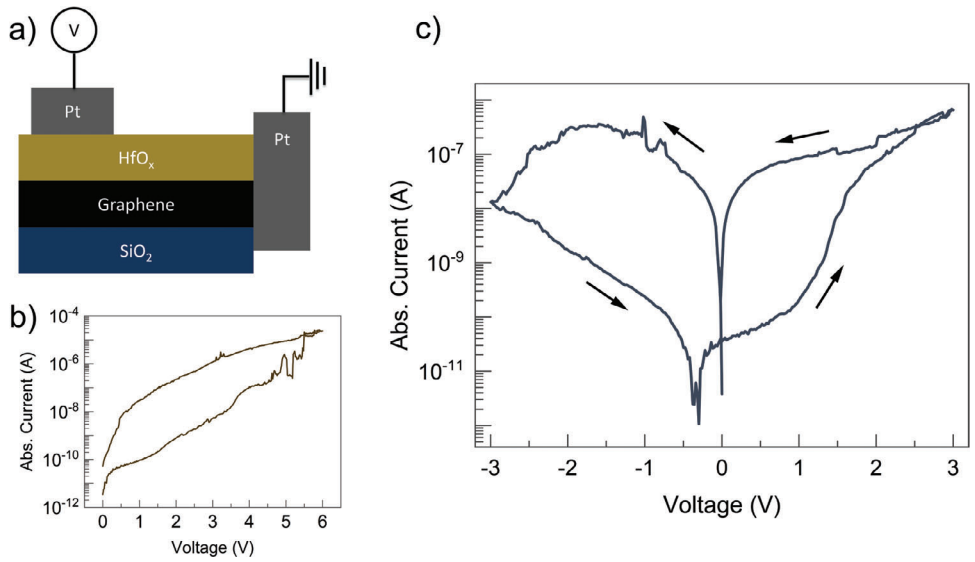

Figure 8. a) Schematic representation of the measured device in side-view. b) *I–V* curve of the electroforming step and c) *I–V* sweep.

graphene was minimized, while the HfO_2 layer was sufficiently oxidized by the oxygen-containing species from the target. Despite the presence of a significant D-band intensity, our results indicate that under the chosen growth conditions the in-plane conductivity of the graphene layer can be preserved, yielding a functional bottom electrode for our memristive devices. Applying this quasi van der Waals approach offers new routes for the heterogeneous integration of oxides and graphene on future device architectures.

4. Experimental Section

Graphene Transfer: The graphene was transferred to SiO_2/Si substrates via a wet transfer method using commercial (Graphenea) chemical-vapour-deposited graphene on Cu foil. The graphene was protected by a PMMA layer during the transfer. The copper foil was dissolved using ammonium persulfate BioChemica ($(NH_4)_2S_2O_8$; AppliChem Panreac, ITW Companies). The surface of the SiO_2/Si substrates was activated using O_2 plasma. After the wet transfer, the graphene was dried using a N_2 and placed on a hotplate (10 min at $T = 150$ °C) to remove any residual water from the interface. In the next step, the PMMA protective layer was removed with acetone and rinsed with isopropanol. Prior to the HfO_2 deposition, potential residual PMMA was removed by annealing the substrates in the pulsed-laser deposition (PLD) chamber (2 h at $T = 600$ °C and $p = 1 \times 10^{-7}$ mbar).

Deposition of HfO_2: The HfO_2 thin films were grown using a PLD system (SURFACE systems+technology GmbH & Co). A KrF excimer laser (COMPex 205F Coherent) with a wavelength of 248 nm was used for the ablation. The backside of the samples was heated directly using an infrared laser. The growth pressure was adjusted, starting from a system base pressure of 1×10^{-7} mbar. A spot size of 2.2 mm^2 and a laser-pulse frequency of 4 Hz were selected for all of the experiments. The samples were cooled to room temperature immediately after the depositions. The deposition pressure, temperature, fluence, and target-to-substrate distance were varied in order to obtain optimal results.

Structural Characterization: Crystallographic properties were investigated by X-ray diffraction (XRD) analysis by performing standard XRD in Bragg–Brentano geometry as well as grazing incidence measurements (GI) using a low (1°) incidence angle (D8 Discover, Bruker AXS GmbH, Karlsruhe, Germany). Cu$K\alpha_1$ radiation ($\lambda = 1.5406$ Å) was used to collect the θ–2θ patterns and the X-ray reflectivity curves that were used to determine the film thickness.

The growth was monitored in situ using a reflection high-energy electron diffraction system (TorrRHEED, Staib Instruments) operated at 35 kV (1.5 µA). The patterns were visualized and analyzed using kSA 400 software (k-Space Associates, Inc.).

Atomic force microscopy (AFM, Nanosurf FlexAFM, C3000) was employed to examine the morphology of the samples. Silicon tips (PPP-NCHR-20, Nanosensors) were used to probe the samples in tapping mode. The AFM images were processed using WSxM 4.0 software.[21]

Raman spectra were acquired with a confocal Raman microscope (Renishaw inVia). A green ($\lambda = 532$ nm) excitation laser (Coherent Compass 315 M 150SL) was used. The laser power was optimized in order to prevent damage to the graphene layer(s), while ensuring sufficiently high intensity for reliable analysis. The Raman signal was collected via an objective lens (50 ×, NA = 0.75, Leica N-plan EPI). The signal was dispersed using a 2400 l mm^{-1} grating and recorded with a CCD camera. The spectral resolution was 1 cm^{-1}. For the curve fitting, the intensity was normalized to 1. Lorentzian (for D and D″) and Breit-Wigner-Fano (for G and D′) line shapes were used for the curve fitting. For the Fano line shapes −0.1 value was used for the $1/q_{BWF}$ coefficient.

Microstructural analysis of the heterostructures was performed by TEM. Cross-sectional TEM lamellae were prepared by FIB milling (Helios NanoLab 400S FIB-SEM, FEI). HR-TEM images were acquired using a spherical aberration-corrected TEM (FEI Titan 80–300 TEM) equipped with a field emission gun and an image Cs-corrector (CEOS CETCOR). The microscope was operated at an acceleration voltage of 80 kV to reduce knock-on damage of the graphene layers.

Electrical Characterization: The resistivity of the as-transferred graphene was measured by wire bonding the graphene to Pt pads using Al wire and sealing the Al/graphene contacts using Pt paste. For contacting the bottom (graphene) electrode a simple line structure was etched into the HfO_2 in three locations, spaced 3–5 mm apart. The depth of the etching trenches was selected such, that the graphene layer was etched through. These were then filled with Pt/(Ti) by means of e-beam evaporation. The deposition rate in the custom-made system was controlled in situ by a crystal oscillator micro balance. This way a side contact to the Gr was produced. The etched line structures were contacted in pairs using W needles in order to measure the resistivity of the graphene across the sample.

Pt/(Ti) pads were also used for the top electrode. These were produced by a lift-off process and also deposited by e-beam evaporation. *I–V* sweeps

were performed with a Keithley 2611A SourceMeter and all voltages were applied to the top electrode. A current compliance of 100 µA (value not reached) was used for the electroforming as well as the switching process. The step size was 20 mV and the holding time before measurement was 5 ms.

Supporting Information

Supporting Information is available from the Wiley Online Library or from the author.

Acknowledgements

Thomas Heisig was gratefully acknowledged for advice and discussions regarding graphene transfer and stability. Thorsten Brazda and David Fabijan were gratefully acknowledged for their help with the Raman setup and fitting of the data, respectively. The authors would also like to thank Niclas Schmidt and Silvia Karthäuser for the valuable discussions regarding the initial growth of HfO_2 on HOPG. This work was funded by Deutsche Forschungsgemeinschaft (DFG) through SFB 917 "Nanoswitches". MW was funded by the DFG (DI 919/8-1) and by the FLAG-ERA project "To2Dox".

Open access funding enabled and organized by Projekt DEAL.

Conflict of Interest

The authors declare no conflict of interest.

Data Availability Statement

The data that support the findings of this study are available from the corresponding author upon reasonable request.

Keywords

pulsed-laser deposition, quasi van der Waals growth, resistive random-access memory, resistive switching

Received: August 12, 2023
Revised: October 27, 2023
Published online: January 17, 2024

[1] R. Dittmann, J. P. Strachan, *APL Mater.* **2019**, *7*, 110903.
[2] R. Waser, R. Dittmann, S. Menzel, T. Noll, *Faraday Discuss.* **2019**, *213*, 11.
[3] T. Guo, B. Sun, S. Ranjan, Y. Jiao, L. Wei, Y. N. Zhou, Y. A. Wu, *ACS Appl. Mater. Interfaces.* **2020**, *12*, 54243.
[4] M. Lanza, A. Sebastian, W. D. Lu, M. Le Gallo, M.-F. Chang, D. Akinwande, F. M. Puglisi, H. N. Alshareef, M. Liu, J. B. Roldan, *Science* **2022**, *80*, 376.
[5] D. V. Christensen, R. Dittmann, B. Linares-Barranco, A. Sebastian, M. Le Gallo, A. Redaelli, S. Slesazeck, T. Mikolajick, S. Spiga, S. Menzel, I. Valov, G. Milano, C. Ricciardi, S.-J. Liang, F. Miao, M. Lanza, T. J. Quill, S. T. Keene, A. Salleo, J. Grollier, D. Marković, A. Mizrahi, P. Yao, J. J. Yang, G. Indiveri, J. P. Strachan, S. Datta, E. Vianello, A. Valentian, J. Feldmann, et al., *Neuromorphic Comput. Eng.* **2022**, *2*, 022501.
[6] Y. Xu, T. Liu, K. Liu, Y. Zhao, L. Liu, P. Li, A. Nie, L. Liu, J. Yu, X. Feng, F. Zhuge, H. Li, X. Wang, T. Zhai, *Nat. Mater.* **2023**, *22*, 1078.
[7] W. Banerjee, A. Kashir, S. Kamba, *Small* **2022**, *18*, 2107575.
[8] S. Brivio, S. Spiga, D. Ielmini, *Neuromorphic Comput. Eng.* **2022**, *2*, 042001.
[9] E. Perez-Bosch Quesada, E. Perez, M. K. Mahadevaiah, C. Wenger, *Neuromorphic Comput. Eng.* **2021**, *1*, 024006.
[10] M. Xiao, C. Qiu, Z. Zhang, L.-M. Peng, *ACS Appl. Mater. Interfaces.* **2017**, *9*, 34050.
[11] P. Zhou, S. Yang, Q. Sun, L. Chen, P. Wang, S. Ding, D. W. Zhang, *Sci. Rep.* **2014**, *4*, 2.
[12] Y. Yan, S. Peng, Z. Jin, D. Zhang, J. Shi, *Crystals* **2022**, *12*, 513.
[13] Y. H. Park, M. H. Kim, S. B. Kim, H. J. Jung, K. Chae, Y. H. Ahn, J.-Y. Park, F. Rotermund, S. W. Lee, *Chem. Mater.* **2016**, *28*, 7268.
[14] D. Diaz-Fernandez, M. Spreitzer, T. Parkelj, D. Suvorov, *Appl. Surf. Sci.* **2018**, *455*, 227.
[15] B. Chen, Z. Jovanovic, S. Abel, P. T. P. Le, U. Halisdemir, M. Smithers, D. Diaz-Fernandez, M. Spreitzer, J. Fompeyrine, G. Rijnders, G. Koster, *ACS Appl. Mater. Interfaces.* **2020**, *12*, 42925.
[16] Z. Jovanovic, U. Trstenjak, H.-C. Ho, O. Butsyk, B. Chen, E. Tchernychova, F. Borodavka, G. Koster, J. Hlinka, M. Spreitzer, *ACS Appl. Mater. Interfaces.* **2023**, *15*, 6058.
[17] L. Dai, G. Niu, J. Zhao, H. Zhao, Y. Liu, Y. Wang, Y. Zhang, H. Wu, L. Wang, D. Pfützenreuter, J. Schwarzkopf, C. Dubourdieu, T. Schroeder, Z.-G. Ye, Y.-H. Xie, W. Ren, *J. Mater. Chem. C.* **2020**, *8*, 3445.
[18] S. A. Lee, J.-Y. Hwang, E. S. Kim, S. W. Kim, W. S. Choi, *ACS Appl. Mater. Interfaces.* **2017**, *9*, 3246.
[19] Z. Lu, X. Sun, M. A. Washington, T.-M. Lu, *J. Phys. D. Appl. Phys.* **2018**, 095301.
[20] S.-H. Bae, K. Lu, Y. Han, S. Kim, K. Qiao, C. Choi, Y. Nie, H. Kim, H. S. Kum, P. Chen, W. Kong, B.-S. Kang, C. Kim, J. Lee, Y. Baek, J. Shim, J. Park, M. Joo, D. A. Muller, K. Lee, J. Kim, *Nat. Nanotechnol.* **2020**, *15*, 272.
[21] H. S. Kum, H. Lee, S. Kim, S. Lindemann, W. Kong, K. Qiao, P. Chen, J. Irwin, J. H. Lee, S. Xie, S. Subramanian, J. Shim, S.-H. Bae, C. Choi, L. Ranno, S. Seo, S. Lee, J. Bauer, H. Li, K. Lee, J. A. Robinson, C. A. Ross, D. G. Schlom, M. S. Rzchowski, C.-B. Eom, J. Kim, *Nature* **2020**, *578*, 75.
[22] J. Kim, C. Bayram, H. Park, C.-W. Cheng, C. Dimitrakopoulos, J. A. Ott, K. B. Reuter, S. W. Bedell, D. K. Sadana, *Nat. Commun.* **2014**, *5*, 4836.
[23] Y. Kim, S. S. Cruz, K. Lee, B. O. Alawode, C. Choi, Y.i Song, J. M. Johnson, C. Heidelberger, W. Kong, S. Choi, K. Qiao, I. Almansouri, E. A. Fitzgerald, J. Kong, A. M. Kolpak, J. Hwang, J. Kim, *Nature* **2017**, *544*, 340.
[24] H. Kum, D. Lee, W. Kong, H. Kim, Y. Park, Y. Kim, Y. Baek, S.-H. Bae, K. Lee, J. Kim, *Nat. Electron.* **2019**, *2*, 439.
[25] H. Yoon, T. K. Truttmann, F. Liu, B. E. Matthews, S. Choo, Q. Su, V. Saraswat, S. Manzo, M. S. Arnold, M. E. Bowden, J. K. Kawasaki, S. J. Koester, S. R. Spurgeon, S. A. Chambers, B. Jalan, *Sci. Adv.* **2022**, *8*.
[26] B. Zou, C. Walker, K. Wang, V. Tileli, O. Shaforost, N. M. Harrison, N. Klein, N. M. Alford, P. K. Petrov, *Growth of Epitaxial Oxide Thin Films on Graphene, Sci. Rep.* **2016**, *6*, 31511.
[27] W. K. Morrow, S. J. Pearton, F. Ren, *Small* **2016**, *12*, 120.
[28] F. Tuinstra, J. L. Koenig, *J. Chem. Phys.* **1970**, *53*, 1126.
[29] A. C. Ferrari, J. C. Meyer, V. Scardaci, C. Casiraghi, M. Lazzeri, F. Mauri, S. Piscanec, D. Jiang, K. S. Novoselov, S. Roth, A. K. Geim, *Raman Spectrum of Graphene and Graphene Layers* **2006**.
[30] X. Tang, N. Reckinger, O. Poncelet, P. Louette, F. Ureña, H. Idrissi, S. Turner, D. Cabosart, J.-F. Colomer, J.-P. Raskin, B. Hackens, L. A. Francis, *Sci. Rep.* **2015**, *5*.
[31] M. M. Lucchese, F. Stavale, E. H. M. Ferreira, C. Vilani, M. V. O. Moutinho, R. B. Capaz, C. A. Achete, A. Jorio, *Carbon N. Y.* **2010**, *48*, 1592.

[32] L. G. Cançado, A. Jorio, E. H. M. Ferreira, F. Stavale, C. A. Achete, R. B. Capaz, M. V. O. Moutinho, A. Lombardo, T. S. Kulmala, A. C. Ferrari, *Nano Lett.* **2011**, *11*, 3190.
[33] X. Zhao, Y. Ando, *Japanese J. Appl. Physics, Part 1 Regul. Pap. Short Notes Rev. Pap.* **1998**, *37*, 4846.
[34] K. N. Kudin, B. Ozbas, H. C. Schniepp, R. K. Prud'homme, I. A. Aksay, R. Car, *Raman Spectra of Graphite Oxide and Functionalized Graphene Sheets* **2023**, *12*, 36.
[35] A. Eckmann, A. Felten, A. Mishchenko, L. Britnell, R. Krupke, K. S. Novoselov, C. Casiraghi, *Nano Lett.* **2012**, *12*, 3925.
[36] N. Schmidt, K. Z. Rushchanskii, U. Trstenjak, R. Dittmann, S. Karthäuser, *ACS Appl. Nano Mater* **2022**, *6*, 148.
[37] L. Wang, I. Meric, P. Y. Huang, Q. Gao, Y. Gao, H. Tran, T. Taniguchi, K. Watanabe, L. M. Campos, D. A. Muller, J. Guo, P. Kim, J. Hone, K. L. Shepard, C. R. Dean, *Science* **2013**, *342*, 614.
[38] L. Anzi, A. Mansouri, P. Pedrinazzi, E. Guerriero, M. Fiocco, A. Pesquera, A. Centeno, A. Zurutuza, A. Behnam, E. A. Carrion, E. Pop, R. Sordan, *Ultra-low contact resistance in graphene devices at the Dirac point, 2D Mater.* **2018**, *5*.
[39] F. Giubileo, A. Di Bartolomeo, *Prog. Surf. Sci.* **2017**, *92*, 143.
[40] J. A. Robinson, M. Labella, M. Zhu, M. Hollander, R. Kasarda, Z. Hughes, K. Trumbull, R. Cavalero, D. Snyder, *Appl. Phys. Lett.* **2011**, *98*, 96.
[41] J. S. Moon, M. Antcliffe, H. C. Seo, D. Curtis, S. Lin, A. Schmitz, I. Milosavljevic, A. A. Kiselev, R. S. Ross, D. K. Gaskill, P. M. Campbell, R. C. Fitch, K.-M. Lee, P. Asbeck, *Appl. Phys. Lett.* **2012**, *100*, 2010.
[42] H. Y. Lee, P. S. Chen, T. Y. Wu, Y. S. Chen, C. C. Wang, P. J. Tzeng, C. H. Lin, F. Chen, C. H. Lien, M. J. Tsai, Low power and high speed bipolar switching with a thin reactive ti buffer layer in robust HfO2 based RRAM, Tech. Dig. – Int. Electron Devices Meet. IEDM **2008**.
[43] W. Kim, S. Menzel, D. J. Wouters, B. Roesgen, J. Robertson, R. Waser, V. Rana, *Nanoscale* **2016**, *8*, 17774.
[44] P. Jancovic, B. Hudec, E. Dobrocka, J. Dérer, J. Fedor, K. Fröhlich, *Appl. Surf. Sci.* **2014**, *312*, 112.
[45] F. Cüppers, S. Menzel, C. Bengel, A. Hardtdegen, M. Von Witzleben, U. Böttger, R. Waser, S. Hoffmann-Eifert, *APL Mater.* **2019**, *7*, 91105.
[46] R. Dittmann, S. Menzel, R. Waser, *Adv. Phys.* **2021**, *70*, 155.
[47] T. Heisig, K. Lange, A. Gutsche, K. T. Goß, S. Hambsch, A. Locatelli, T. O. Mentes, F. Genuzio, S. Menzel, R. Dittmann, *Adv. Electron. Mater.* **2022**, *8*, 2100936.
[48] C. Baeumer, C. Schmitz, A. Marchewka, D. N. Mueller, R. Valenta, J. Hackl, N. Raab, S. P. Rogers, M. I. Khan, S. Nemsak, M. Shim, S. Menzel, C. M. Schneider, R. Waser, R. Dittmann, *Nat. Commun.* **2016**, *7*, 12398.
[49] A. C. Ferrari, J. Robertson, *Phys. Rev. B.* **2000**, *61*, 14095.